


Probing free carrier plasmons in doped semiconductors using spatially resolved electron energy loss spectroscopy

Hongbin Yang ^{1,*}, Eric L. Garfunkel,² and Philip E. Batson³

¹*Department of Chemistry and Chemical Biology, Rutgers University, Piscataway, New Jersey 08854, USA*

²*Department of Chemistry and Chemical Biology, Department of Physics and Astronomy, Rutgers University, Piscataway, New Jersey 08854, USA*

³*Department of Physics and Astronomy, Department of Materials Science and Engineering, Rutgers University, Piscataway, New Jersey 08854, USA*

 (Received 28 May 2020; revised 25 October 2020; accepted 3 November 2020; published 30 November 2020)

We report spatially resolved measurements of free carrier collective excitations in a doped semiconductor. Using ~ 10 meV resolution electron energy loss spectroscopy (EELS) in an electron microscope with \AA spatial resolution, we identify both surface and bulk carrier plasmons at infrared energies in a freestanding film of indium tin oxide (ITO). The interference patterns of long wavelength propagating surface carrier plasmons are revealed using spatially resolved EELS, from which we extract a dispersion relation. We further show that the energies of these plasmons vary near the surfaces and grain boundaries of the film due to band bending. Modeling based on dielectric theory agrees very well with experimental results. Finally, carrier plasmons in amorphous and crystalline ITO films are compared. These results should also be helpful for understanding the free carrier plasmons in other doped semiconductors in nanoscale volumes.

DOI: [10.1103/PhysRevB.102.205427](https://doi.org/10.1103/PhysRevB.102.205427)

I. INTRODUCTION

Plasmons, collective excitations of charged particles, are fundamental many-body properties of solids [1–3]. The contributing charged ensemble can be composed of the valence electrons of the solid or charge carriers introduced into the material from dopants. In contrast to plasmons of valence electrons which usually occur above ~ 10 eV, plasmons of free carriers typically take place in the infrared (IR) or terahertz (THz) regime as a result of the low dopant solubility [4]. Plasmons of free carriers (carrier plasmons) in doped semiconductors have been subjects of considerable interest for both fundamental and applied research [5]. Investigations of these plasmons have helped elucidate fundamental aspects of semiconductors that are important for their transport and optical properties [6]. In addition, semiconductor carrier plasmons can interact strongly with phonons, interband excitations, and surface states of a solid [7,8]. The unique properties of these plasmons, such as highly tunable plasma frequency through doping or electrical field, and stronger field confinement at low energy than noble metal plasmons, have also made them promising for applications in sensing, telecommunications, metamaterials, etc. [9–12].

Because of their low energies, previous experiments on semiconductor carrier plasmons have relied on techniques with high energy resolution but average over millimeter or micrometer sized regions [6,8]. Although spatially resolved electron energy loss spectroscopy (EELS) can measure plasmons at nanometer scale, the energy resolution of this technique was limited in the past by the natural line width

of field emission electron sources, commonly used in small electron beam systems. Most prior studies have focused on plasmons of valence electrons, where the resonances occur at high energies and are relatively intense [13,14]. Carrier plasmons in doped semiconductors remain less explored by spatially resolved EELS. In particular, the relative scattering intensity of surface and bulk carrier plasmons were not well understood in some earlier studies, in part due to the insufficient energy resolution [15–17]. The bulk mode is of particular interest here because it allows one to determine the density of free carriers [18], an important quantity for many semiconductor devices. Moreover, the effects of surface band bending on free carriers plasmons were not considered in previous STEM-EELS works [15–17,19,20].

Recent developments in scanning transmission electron microscope (STEM) instrumentation have drastically improved the energy resolution of transmission EELS, thus enabling spatially resolved studies of various low energy excitations [21–26]. Despite some successes using scanning probe measurements [27,28], fast electrons can achieve much better spatial resolution, probe a wider range of energy and momentum, and couple to both surface and bulk excitations.

In this work, we aim to (i) measure free carrier plasmons with high energy and spatial resolution and (ii) understand quantitatively the energy loss of keV electrons due to excitation of these plasmons. We choose tin doped indium oxide (ITO) as a model system in our study for its well characterized optical properties and free-electron-like carriers [29]. Using STEM-EELS equipped with a source monochromator, we launch and detect both surface and bulk modes of carrier plasmons in a freestanding film of ITO. The interaction of these plasmons with the surfaces, edges, and grain boundaries of the film are shown explicitly by EELS mapping with high

*hongbin.yang@rutgers.edu

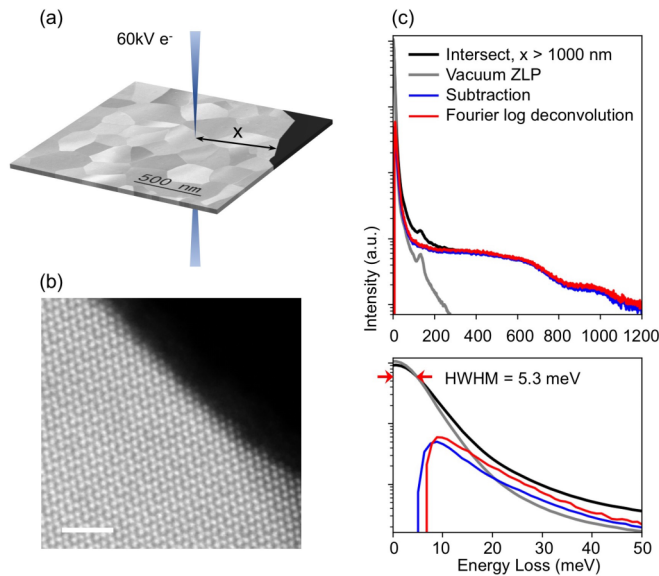


FIG. 1. (a) Schematic of the STEM-EELS experiment, produced using a medium angle annular dark field (MAADF) image of the ITO film; the arrow identifies the nearest distance to the film edge. (b) A high angle annular dark field (HAADF) image for a grain oriented near its [110] zone axis. The scale bar denotes 2 nm. (c) Top panel: EELS taken when an electron beam intersects the ITO film but far away from the film edge (black), in vacuum far away from any specimen (gray), difference spectrum between the two (blue) and the result after Fourier log deconvolution (red). The peak at around 130 meV is due to the monochromator slit contamination. Bottom panel: zoomed-in view of the top panel for energy loss between 0 to 50 meV, showing the choice of methods for background removal result in negligible differences for energy loss above 10 meV. The red arrows indicate the energy resolution of better than 11 meV. Intensities are shown in logarithmic scale for both panels.

spatial resolution. We model our results based on dielectric theory and quantify the energy, scattering probabilities, and damping of these plasmons. Dispersion relation of the surface plasmons was extracted from experiments. Finally, we show the effects of dopant activation on the density of free carriers by comparing the plasmons in amorphous and crystalline ITO film. These findings will advance our understanding of low energy electronic excitations in many other materials at the nanometer scale.

II. METHODS

The ITO films studied in this work were deposited by direct current sputtering. During deposition, a glass substrate with a soluble carbon top layer was kept at room temperature. As deposited amorphous ITO film was then removed from substrate and transferred onto a lacey carbon supported TEM grid. Polycrystalline ITO film was obtained by annealing the grid with film under vacuum at 400 °C, for about 10 minutes.

STEM imaging and EELS acquisition were performed using a Nion UltraSTEM 100. The electron microscope was operating at 60 kV and is equipped with a high-resolution source monochromator and an aberration corrector. In our experiment, fast electrons were focused to a 1.5 to 2 Å spot

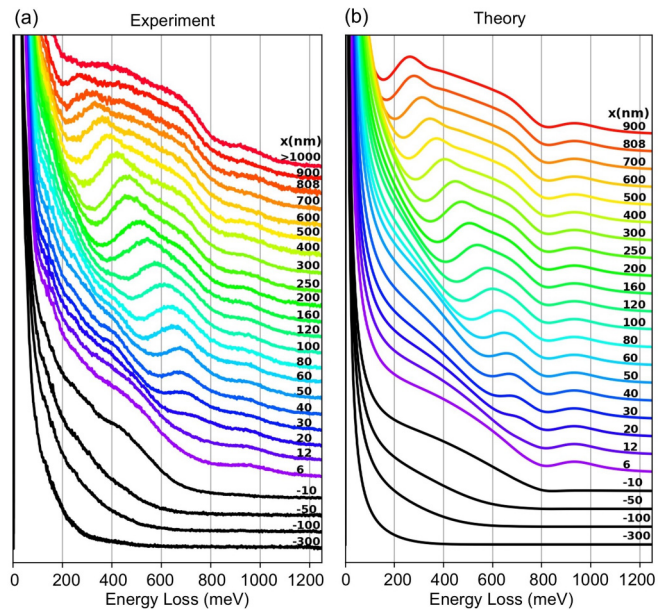


FIG. 2. Experimental (a) and theoretical (b) EEL spectra taken at varying distances from the film edge shown in rainbow colors. A loop spectra (taken outside the film edge) are shown in black.

before passing through the specimen, with a half convergence angle of 30 mrad. The energy resolution, measured at the full width of half maximum (FWHM) of the zero-loss peak (ZLP) in vacuum, was in the range of 10 to 14 meV when the monochromator is used. Another benefit the monochromator offers is the reduced intensity of ZLP tail in the IR energy range. The full width at 1/1000 maximum of the ZLPs were around 120 meV in our experiments. EELS signals were collected through a 16 mrad half angle aperture on the optical axis. Probe current right after beam flash was about 60 pA, which will be reduced to about 5 pA if the monochromator slit is introduced. Detector gain was corrected for each spectrum. The elastic scattering background can be removed either by subtracting a ZLP in vacuum far away from any specimen or by Fourier log deconvolution [30]. These two methods produce almost identical results for energy loss above 10 meV, as shown in Fig. 1(c). Although EELS signals were seen as low as 10 meV after background removal, in this paper we focus on those above 100 meV.

III. RESULTS AND DISCUSSION

A typical area of the crystalline ITO film is shown in Figs. 1(a) and 1(b); the lateral grain sizes are in the range of 50 to 400 nm, with a thickness of about 24 nm. The tin percentage of the ITO film is about 10%, as measured by x-ray photoemission spectroscopy. Figure 2(a) displays the background subtracted EEL spectra taken at varying distances from the specimen edge. The spectra taken 1000 nm away or further from the edge were almost identical. But when spectra are taken closer to the edge, the scattering intensities vary significantly between about 180 to 700 meV. These are the surface carrier plasmons. Their contribution to the total energy loss intensity gradually decreases as the beam moves even closer to the film edge. When the distance is less than about

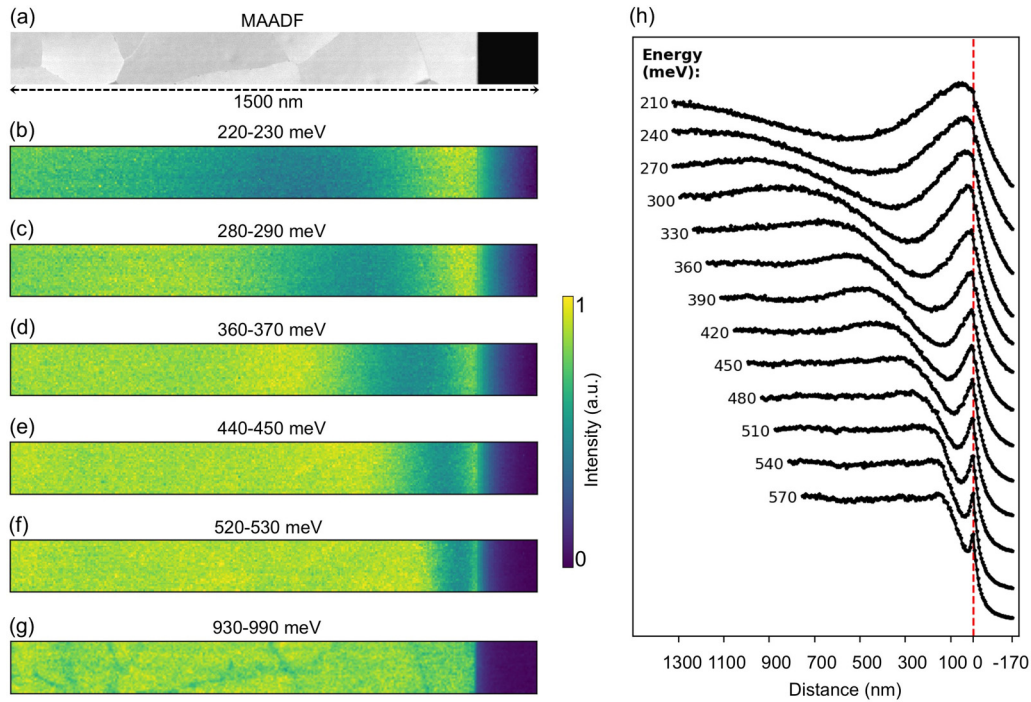


FIG. 3. Spectral images of the surface and bulk carrier plasmons. (a) A MAADF-STEM image of the area where the spectrum images were taken. (b)–(f) Spectral images of the SPPs generated by integrating the spectrum at each pixel within the cited energy range. (f) Spectral image integrated in the bulk carrier plasmon energy range. (h) Intensity line profiles along the long side of the image at various energies.

100 nm, EELS intensities are dominated by an edge mode [31]. The energy loss peak around 950 meV is attributed to the bulk carrier plasmon, where $\text{Re}[\epsilon_{\text{ITO}}(\omega)] = 0$. The lower spectra, taken by placing the electron beam in the vacuum just outside the ITO film edge, show energy loss only to the edge and surface modes. These line shapes are independent of the grain orientation, as long as they are taken at the same distance away from the film edge.

The spatial distributions of these excitations offer more insight into the origin of the variations in the EELS intensities. Spectral images were acquired in a rectangular region that includes both the ITO film and the vacuum, as shown in Fig. 3(a). A spectrum was taken at each pixel while the electron beam scans the 1500×150 nm area, using a pixel size of 5×5 nm. After normalizing the ZLP at each pixel, the spatial variation in the scattering intensities at different energies can be visualized. Spectral images in several energy ranges are presented in Figs. 3(b)–3(f). These are the interference patterns of the surface plasmon polaritons (SPPs), coupled two-dimensional charge oscillations along the top and bottom surfaces of the film. As fast electrons travel through the ITO film, SPPs are launched and propagate outward. When the SPPs reach the boundary of the ITO film, they are reflected and propagate back towards the incoming wave. The scattering intensity is therefore either enhanced or reduced, for constructive or destructive interference, respectively. The distance from the position of electron impact to the nearest ITO film edge therefore determines the overall spectral shape. The scattering intensities modulate along the direction perpendicular to the film edge, with two intensity maxima in each spectral image, the distance

between which corresponds to half of the SPP wavelength. Our result is somewhat analogous to the observations of surface plasmon interference patterns in gated graphene by optical near-field experiments [32,33]. In our case, however, SPPs with a wide range of wave vectors and energies are excited.

As the energy increases and approaches the surface plasmon energy, $\hbar\omega_{\text{SP}}$, the SPPs have shorter wavelengths and larger wave vectors. This makes the evanescent field associated with the surface plasmons decay quicker into vacuum [34,35] producing sharper edge features in Fig. 3(h). Inside the ITO film, modulations in scattering intensities are mainly observed close to the edge, suggesting that the damping of SPPs is strong in our ITO films. This is rather different from those observed in silver nanowires, although their $\text{Im}[\epsilon(\omega)]$ in the IR range are comparable [34,36,37]. We think this may not only result from optical loss intrinsic to the materials [38,39] but also from the differences in specimen geometry, e.g. 2D vs 1D [40].

In contrast to the surface carrier plasmons, the intensities of the bulk carrier plasmons drop abruptly at the film edge. Moreover, as shown in Fig. 3(f), contrast variations, present as differences in scattering intensity, was seen near the grain boundaries. By comparing spectra taken at the grain boundary and as one moves away from the boundary, plotted in Fig. 4(a), we find the bulk carrier plasmons near grain boundaries shift to lower energy, which is responsible for the contrast variations. The variations in plasmon energy are primarily due to the changes in plasma frequency near the long wavelength limit. We further find that the amount of this decrease is sensitive to the extent of structural disorder at the

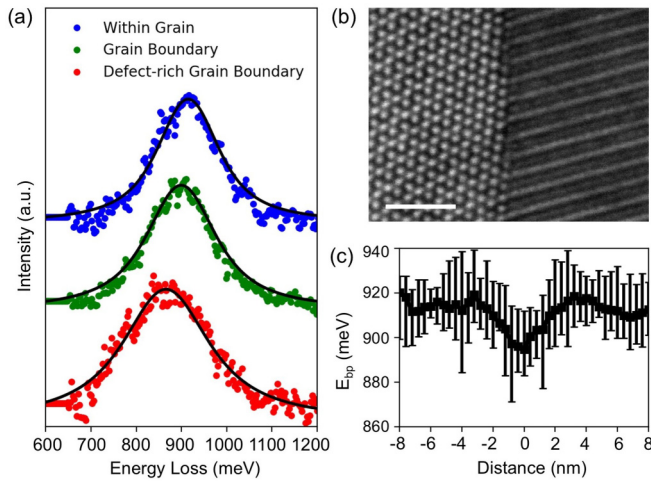


FIG. 4. Carrier plasmons near grain boundaries. (a) Bulk carrier plasmons from inside the grains (blue), at an atomically sharp grain boundary (green) and at a defect-rich grain boundary (red). The bulk contribution shown here is extracted by subtracting an exponential background. These spectra were modeled using a bulk energy loss function (black curves shown superimposed). (b) A HAADF-STEM image of an atomically sharp grain boundary. The green spectrum in (a) is taken at this grain boundary. The scale bar denotes 2 nm. The grain on the left is imaged along its [110] axis. (c) Line profile of bulk carrier plasmon energy across the grain boundary shown in (b). Error bars in energy were determined from six separate measurements at different regions along the same grain boundary.

grain boundary. For instance, a 20 meV decrease is observed at an atomically sharp grain boundary, shown in Fig. 4(b). The redshift can increase to up to about 60 meV for defect-rich grain boundaries. A line profile in Fig. 4(c) taken with 4 Å spatial resolution shows the plasmon energy recovers to the bulk value of adjacent grains within 3 nm from the boundary. Reduced valence plasmons energies have been observed at the grain boundaries in Al and SrTiO₃ by STEM-EELS, which were attributed to the decreased valence electron densities [41–43]. Here, we think the change in plasmon energies is due to the reduction of free carrier density in and near grain boundaries [44,45]. The extra defect states at the grain boundaries are likely to be the cause for this [46]. But we note that no appreciable tin segregation has been found by our core-loss EELS measurements at these grain boundaries, in contrast to Ref. [47].

Theoretical spectra were calculated to further interpret our observations. The free carriers in our In₂O₃:Sn system originate mainly from the dopant Sn. These carrier electrons occupy the conduction band minima of ITO and can be treated by the Drude model:

$$\epsilon(\omega) = \epsilon_{\infty} - \frac{\omega_p^2}{\omega^2 + i\gamma\omega}, \quad (1)$$

where $\omega_p = \sqrt{ne^2/m^*\epsilon_0}$ is the plasma frequency of the free carriers with density n . Here the effective mass of conduction band electrons m^* is taken to be $0.35 m_0$, a value commonly found for ITO at this doping level [48]. Semiconductors often have interband transitions occurring at energies above the plasma frequency of their free carriers. This leads to a

background dielectric constant ϵ_{∞} for the collective motions of the carrier electrons. One should therefore expect that the bulk loss occurs close to $\hbar\omega_p/\sqrt{\epsilon_{\infty}}$, the screened plasma frequency.

Based on classical dielectric response theory, the differential scattering probability $P(k, \omega)$ was calculated for an ITO film infinite in the (x, y) plane [49,50]. We see that for a thin film the symmetric coupled surface plasmons instead of the bulk mode dominate scattering intensities. The bulk carrier plasmon dispersion curve crosses the Bethe ridge, defined by $E = \hbar^2/m^*(k^2 + 2kk_F)$, at $k_c = 1.3 \text{ nm}^{-1}$, where we find the critical wave vector [51]. This value is about 10 times smaller than that of the 15 eV bulk plasmons in Al [52], suggesting that the range of wave vectors for carrier plasmons in semiconductors to be well defined is much narrower, as can be expected from the low density of carrier electrons. Theoretical spectra can then be obtained by integrating in momentum. We found spectra taken $> 1000 \text{ nm}$ from the edge resemble the theoretical spectrum for an infinite ITO film [50]. In order to account for the effect of the film termination on the modulations in scattering intensities, a phenomenological model for wave reflection and interference has been adopted [53–55].

$$x > 0: \Gamma(x, \omega) = \int_0^{k_c} k dk P(k, \omega) [1 + \cos(2kx + \phi_r)] \quad (2)$$

We calculate $\Gamma(x, \omega)$ for the relevant energy range, with x being the distances from the edge where the spectra were taken. Excellent agreement was found between theory and experiment [Figs. 2(a) and 2(b)] for x in the range of 900 to 100 nm. The exact energy of the energy loss peak is governed by the distance x and phase shift ϕ_r upon reflection. From equation (2), constructive interferences occur when the cosine term equals to 1. As we find the phase shift ϕ_r is small [50], this condition is fulfilled when $m\lambda_{\text{SPP}} = 2x$, where λ_{SPP} is the SPP wavelength. The integer $m = 1, 2, 3$, is commonly called the order of the resonant modes. In our experiments, both dipolar and multipolar surface plasmons resonances are excited. The dipolar resonances occur when $m = 1$, so that their wavelengths are roughly twice the distance x . These resonances define the energy of the asymmetric peak in our spectra, which are used to obtain the dispersion relation shown in Fig. 5. The scattering signals that appear on the high energy side of the dipolar resonance originate from multipolar surface plasmon resonances ($m > 1$). These higher order ones are not seen as individual peaks for several reasons. First, the low plasma frequency of ITO compared to metals makes the neighboring resonant modes close in energy, especially for the multipolar resonances. Second, plasmons in our film geometry are different from the Fabry-Pérot type resonance in that the reflection occurs only from the film edge in one direction, instead of two reflectors on both ends [36,56]. Third, the damping of these SPPs is relatively strong. As shown in Fig. 6(a), $\hbar\gamma \approx 190 \text{ meV}$ gives a good fit to our data.

Fast electrons can also excite edge modes in addition to the coupled surface plasmons, when passing very close to the film edge. These are the plasmon polaritons propagating along the edges of the ITO film. Although the exact energy of these modes needs to be determined by numerical calculation [57], a qualitative understanding can be obtained from the size and

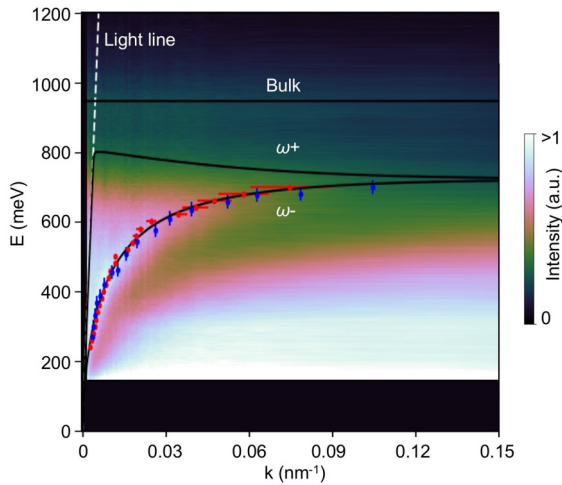


FIG. 5. Dispersion curves of surface and bulk carrier plasmons. The symmetric and antisymmetric modes of coupled surface plasmons and bulk plasmons are labeled as ω^- and ω^+ and Bulk, respectively. Light line in vacuum is shown in white dashed line. Experimental scattering intensities above 150 meV are shown as color coded background as functions of π/x (horizontal axis) and energy (vertical axis). Data points in blue are taken from the peak energy from spectra in Fig. 2(a), with an error bar of ± 20 meV. Data points in red are measured from the distances between maxima in Fig. 3(g), with an error bar of ± 10 nm.

geometry of the specimen. Here the large horizontal size of the ITO film supports long wavelength plasmon polaritons propagating along the edge in the y direction. Excitation of these plasmons produces the intense energy loss features at low energies in Fig. 2(a). Nevertheless, we were able to calculate theoretical spectra for $x < 100$ nm considering only coupled surface and bulk modes and found that the theory agrees reasonably well with experiments. The aloof spectra in Fig. 2(b) were calculated considering only the surface mode.

The dispersion relations of the surface carrier plasmons were extracted from our experiments. We found the relationship between surface plasmon energy and wave vector (π/x) by measuring the dipolar surface plasmon peak energy at each distance. Alternatively, equivalent information can also be obtained by measuring the distance between the two intensity maxima in the spectral images integrated at each energy. Figure 5 shows the theoretical plasmon dispersions of both the surface and bulk modes for an infinite ITO film including the retardation effect [58,59]. Data points obtained by both methods fall close to the theoretical dispersion curve of the symmetric surface plasmons. Normalized experimental energy loss intensities are directly plotted as an image in Fig. 5. One also sees that the strong scattering tracks the surface symmetric plasmon mode. Wave interference is the reason why we are able to observe the dispersion curve from a momentum integrated measurement. Our approach allows probing dispersions with great momentum resolution.

The ability of fast electrons to couple with both surface and bulk excitations allows the surface and bulk screened plasmon energies to be determined independently, which reveals the presence of surface band bending. In Fig. 5, the surface

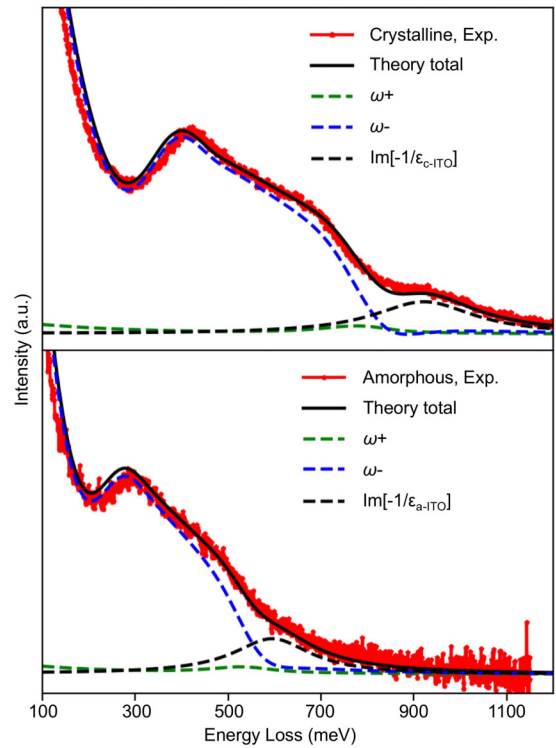


FIG. 6. Carrier plasmons in the crystalline (top) and the amorphous (bottom) ITO films. Both spectra were taken at $x = 400$ nm from the corresponding film edge. Theoretical spectra are shown superimposed in black solid lines. Contribution of the symmetric and antisymmetric modes of coupled surface plasmons and bulk plasmons are also shown separately as labeled.

plasmon dispersion curves approach to $\hbar\omega_{SP}$ at 720 meV. This value is 80 to 100 meV lower than the surface plasma frequency we would expect based on the dielectric function that we have measured [50]. We believe that the depletion layers on the top and bottom surfaces, common for such a film [46], are very likely responsible for this. Once the charge carriers near surfaces are trapped in the surface states, they do not participate in the collective oscillations at the same frequency as those free carriers. Therefore the effective carrier densities near the surfaces are reduced [60–62]. The bulk carrier concentration of our ITO film is about $8.5 \times 10^{20} \text{ cm}^{-3}$, corresponding to a depletion layer width of around 1 nm [44]. By including a layer with lower carrier concentration on both surfaces, our experimental results can be modeled better. For semiconducting materials with a lower doping level, the depletion or accumulation layer width can easily exceed the specimen thickness commonly seen in transmission electron microscopy. This will lead to an inhomogeneous carrier density distribution across the whole specimen [63,64]. The resulting changes on the scattering of fast electrons are left for future work.

Finally, we show that the dopants in crystalline ITO impacts the carrier concentration and plasmons much more so than those in amorphous ITO. Figure 6 compares the plasmons of free carriers in the polycrystalline and amorphous ITO films. Although having similar spectral shape, the energy

of both surface and bulk carrier plasmons are decreased significantly in the as deposited amorphous ITO films. With the theoretical approach described above, we have modeled these EEL spectra and quantified the carrier densities in both films. For the amorphous film, bulk carrier plasmon loss occurs at about 600 meV, in contrast to 940 meV for the crystalline film. This corresponds to an increase in carrier density from about 3.5×10^{20} to $8.5 \times 10^{20} \text{ cm}^{-3}$, agrees well with Hall measurements reported for such films [65]. These increased free carriers mainly originated from the activated Sn donors through the crystallization process [66]. However, less than 40% of the dopants are activated, even if we assume all of the carriers come from Sn instead of oxygen vacancies. It is also interesting to note that the surface plasmon damping we found by modeling is slightly less for the amorphous film (176 meV) than the polycrystalline one (191 meV). These free carriers still follow a Fermi-Dirac distribution at room temperature, as opposed to a Boltzmann distribution, which applies to semiconductors with lower doping. However, their de Broglie wavelengths are on the order of 1 to 3 nm, much larger than the electron wavelength in metals or common atomic spacing, which is the reason why structure disorder contributes little to the carrier scattering, in contrast to metals [67,68]. These results show that the effects of doping on electronic and optical properties can be directly determined with high spatial resolution by STEM-EELS, which will be particularly useful to relate the local structure-property relationships near defects or impurities.

IV. CONCLUSIONS

In summary, the plasmons of free carriers in a doped semiconductor have been thoroughly studied using STEM-EELS with high energy resolution. We have imaged the spatial variation of these plasmons due to the interactions with the film boundaries and described how these interactions modify the energy loss of keV electrons. The surface plasmon dispersion relation, damping, and bulk plasma frequency of an ITO film were extracted experimentally and modeled very well based on dielectric theory. Our results have also demonstrated the possibility to characterize local effects of doping in a nanometer sized region using fast electrons. With the continuous improvement in energy resolution and detection abilities, state-of-the-art STEM-EELS should be able to investigate the low energy carrier plasmons in a wider range of materials and their coupling with other excitations.

ACKNOWLEDGMENTS

The authors are grateful for the valuable comments from Dr. A. Konečná and Prof. T. Gustafsson, Prof. L. Feldman, and Prof. P. Nordlander. H.Y. thanks X. Liu, F. Rebolledo, Prof. J. Zahn and Prof. S. Rangan for their help during sample preparation and Dr. R. Thorpe and Dr. H. Hijazi for the RBS measurements. The authors acknowledge the financial support of the US Department of Energy, Office of Science, Basic Energy Sciences under Award No. DE-SC0005132.

-
- [1] D. Pines and D. Bohm, *Phys. Rev.* **85**, 338 (1952).
 [2] R. H. Ritchie, *Phys. Rev.* **106**, 874 (1957).
 [3] D. Pines and P. Nozières, *Theory of Quantum Liquids* (Addison-Wesley, Redwood City, 1966), pp. 204–223.
 [4] J. M. Luther, P. K. Jain, T. Ewers, and A. P. Alivisatos, *Nat. Mater.* **10**, 361 (2011).
 [5] J. A. Fauchaux, A. L. D. Stanton, and P. K. Jain, *J. Phys. Chem. Lett.* **5**, 976 (2014).
 [6] M. Cardona and G. Güntherodt, *Light Scattering in Solids IV Electronic Scattering, Spin Effects, SERS, and Morphic Effects* (Springer Berlin, Berlin, 1984), pp. 53–69.
 [7] B. B. Varga, *Phys. Rev.* **137**, A1896 (1965).
 [8] H. Lüth, *Surf. Sci.* **126**, 126 (1983).
 [9] A. Agrawal, S. H. Cho, O. Zandi, S. Ghosh, R. W. Johns, and D. J. Milliron, *Chem. Rev.* **118**, 3121 (2018).
 [10] A. Agarwal, M. S. Vitiello, L. Viti, A. Cupolillo, and A. Politano, *Nanoscale* **10**, 8938 (2018).
 [11] T. Taliercio and P. Biagioni, *Nanophotonics* **8**, 949 (2019).
 [12] L. Min, W. Wang, L. Huang, Y. Ling, T. Liu, J. Liu, C. Luo, and Q. Zeng, *Sci. Rep.* **9**, 17622 (2019).
 [13] Y. Wu, G. Li, and J. P. Camden, *Chem. Rev.* **118**, 2994 (2018).
 [14] A. Polman, M. Kociak, and F. J. Garcia de Abajo, *Nat. Mater.* **18**, 1158 (2019).
 [15] H. Matsui, S. Furuta, and H. Tabata, *Appl. Phys. Lett.* **104**, 211903 (2014).
 [16] A. Agrawal, A. Singh, S. Yazdi, A. Singh, G. K. Ong, K. Bustillo, R. W. Johns, E. Ringe, and D. J. Milliron, *Nano Lett.* **17**, 2611 (2017).
 [17] C. S. Granerød, S. R. Bilden, T. Aarholt, Y.-F. Yao, C. C. Yang, D. C. Look, L. Vines, K. M. Johansen, and O. Prytz, *Phys. Rev. B* **98**, 115301 (2018).
 [18] A. J. McAlister and E. A. Stern, *Phys. Rev.* **132**, 1599 (1963).
 [19] G. Bertoni, Q. Ramasse, R. Brescia, L. De Trizio, F. De Donato, and L. Manna, *ACS Mater. Lett.* **1**, 665 (2019).
 [20] S. H. Cho, K. M. Roccapriore, C. K. Dass, S. Ghosh, J. Choi, J. Noh, L. C. Reimnitz, S. Heo, K. Kim, K. Xie, B. A. Korgel, X. Li, J. R. Hendrickson, J. A. Hachtel, and D. J. Milliron, *J. Chem. Phys.* **152**, 014709 (2020).
 [21] O. L. Krivanek, T. C. Lovejoy, N. Dellby, T. Aoki, R. W. Carpenter, P. Rez, E. Soignard, J. Zhu, P. E. Batson, M. J. Lagos, R. F. Egerton, and P. A. Crozier, *Nature (London)* **514**, 209 (2014).
 [22] M. J. Lagos, A. Trugler, U. Hohenester, and P. E. Batson, *Nature (London)* **543**, 529 (2017).
 [23] C. Dwyer, T. Aoki, P. Rez, S. L. Y. Chang, T. C. Lovejoy, and O. L. Krivanek, *Phys. Rev. Lett.* **117**, 256101 (2016).
 [24] P. Rez, T. Aoki, K. March, D. Gur, O. L. Krivanek, N. Dellby, T. C. Lovejoy, S. G. Wolf, and H. Cohen, *Nat. Commun.* **7**, 10945 (2016).
 [25] K. C. Smith, A. Olafsson, X. Hu, S. C. Quillin, J. C. Idrobo, R. Collette, P. D. Rack, J. P. Camden, and D. J. Masiello, *Phys. Rev. Lett.* **123**, 177401 (2019).

- [26] Y. Wu, Z. Hu, X.-T. Kong, J. C. Idrobo, A. G. Nixon, P. D. Rack, D. J. Masiello, and J. P. Camden, *Phys. Rev. B* **101**, 085409 (2020).
- [27] S. Yoshida, Y. Kanitani, R. Oshima, Y. Okada, O. Takeuchi, and H. Shigekawa, *Phys. Rev. Lett.* **98**, 026802 (2007).
- [28] A. J. Huber, F. Keilmann, J. Wittborn, J. Aizpurua, and R. Hillenbrand, *Nano Lett.* **8**, 3766 (2008).
- [29] H. Khamh, E. Sacht, K. Kelly, J.-P. Maria, and S. Franzen, *J. Mater. Chem. C* **6**, 8326 (2018).
- [30] D. W. Johnson and J. C. H. Spence, *J. Phys. D* **7**, 771 (1974).
- [31] A. Konečná, K. Venkatraman, K. March, P. A. Crozier, R. Hillenbrand, P. Rez, and J. Aizpurua, *Phys. Rev. B* **98**, 205409 (2018).
- [32] Z. Fei, A. S. Rodin, G. O. Andreev, W. Bao, A. S. McLeod, M. Wagner, L. M. Zhang, Z. Zhao, M. Thiemens, G. Dominguez, M. M. Fogler, A. H. Castro Neto, C. N. Lau, F. Keilmann, and D. N. Basov, *Nature (London)* **487**, 82 (2012).
- [33] J. Chen, M. Badioli, P. Alonso-Gonzalez, S. Thongrattanasiri, F. Huth, J. Osmond, M. Spasenovic, A. Centeno, A. Pesquera, P. Godignon, A. Z. Elorza, N. Camara, F. J. Garcia de Abajo, R. Hillenbrand, and F. H. Koppens, *Nature (London)* **487**, 77 (2012).
- [34] D. Rossouw and G. A. Botton, *Phys. Rev. Lett.* **110**, 066801 (2013).
- [35] P. Batson, *Ultramicroscopy* **11**, 299 (1983).
- [36] D. Rossouw, M. Couillard, J. Vickery, E. Kumacheva, and G. A. Botton, *Nano Lett.* **11**, 1499 (2011).
- [37] J. Kim, G. V. Naik, A. V. Gavrilenko, K. Dondapati, V. I. Gavrilenko, S. M. Prokes, O. J. Glembocki, V. M. Shalaev, and A. Boltasseva, *Phys. Rev. X* **3**, 041037 (2013).
- [38] S. Franzen, *J. Phys. Chem. C* **112**, 6027 (2008).
- [39] G. V. Naik, J. Kim, and A. Boltasseva, *Opt. Mater. Express* **1**, 1090 (2011).
- [40] Y. Li, K. Zhao, H. Sobhani, K. Bao, and P. Nordlander, *J. Phys. Chem. Lett.* **4**, 1352 (2013).
- [41] A. F. Wright and S. R. Atlas, *Phys. Rev. B* **50**, 15248 (1994).
- [42] P. Nandi, X. Sang, E. R. Hoglund, R. R. Unocic, D. A. Molodov, and J. M. Howe, *Phys. Rev. Materials* **3**, 053805 (2019).
- [43] K. van Benthem, G. Tan, L. K. DeNoyer, R. H. French, and M. Rühle, *Phys. Rev. Lett.* **93**, 227201 (2004).
- [44] O. Zandi, A. Agrawal, A. B. Shearer, L. C. Reimnitz, C. J. Dahlman, C. M. Staller, and D. J. Milliron, *Nat. Mater.* **17**, 710 (2018).
- [45] B. S. Hoener, H. Zhang, T. S. Heiderscheit, S. R. Kirchner, A. S. De Silva Indrasekara, R. Baiyasi, Y. Cai, P. Nordlander, S. Link, C. F. Landes, and W.-S. Chang, *J. Phys. Chem. Lett.* **8**, 2681 (2017).
- [46] S. Dasgupta, M. Lukas, K. Dössel, R. Kruk, and H. Hahn, *Phys. Rev. B* **80**, 085425 (2009).
- [47] H. Morikawa, H. Kurata, and M. Fujita, *J. Electron Microsc.* **49**, 67 (2000).
- [48] I. Hamberg and C. G. Granqvist, *J. Appl. Phys.* **60**, R123 (1986).
- [49] E. Kröger, *Z. Phys.* **235**, 403 (1970).
- [50] See Supplemental Material at <http://link.aps.org/supplemental/10.1103/PhysRevB.102.205427> for (I) theoretical electron energy loss probabilities for an infinite ITO film, (II) theoretical electron energy loss probabilities near an ITO film termination, (III) dopant percentage from x-ray photoelectron spectroscopy, and (IV) infrared reflection measurement and the Drude dielectric function.
- [51] G. Abstreiter, R. Trommer, M. Cardona, and A. Pinczuk, *Solid State Commun.* **30**, 703 (1979).
- [52] P. E. Batson and J. Silcox, *Phys. Rev. B* **27**, 5224 (1983).
- [53] M. Kuttge, E. J. R. Vesseur, A. F. Koenderink, H. J. Lezec, H. A. Atwater, F. J. García de Abajo, and A. Polman, *Phys. Rev. B* **79**, 113405 (2009).
- [54] D. T. Schoen, A. C. Atre, A. Garcia-Etxarri, J. A. Dionne, and M. L. Brongersma, *Nano Lett.* **15**, 120 (2015).
- [55] A. A. Govyadinov, A. Konecna, A. Chuvilin, S. Velez, I. Dolado, A. Y. Nikitin, S. Lopatin, F. Casanova, L. E. Hueso, J. Aizpurua, and R. Hillenbrand, *Nat. Commun.* **8**, 95 (2017).
- [56] J. Martin, M. Kociak, Z. Mahfoud, J. Proust, D. Gerard, and J. Plain, *Nano Lett.* **14**, 5517 (2014).
- [57] F. J. García de Abajo and J. Aizpurua, *Phys. Rev. B* **56**, 15873 (1997).
- [58] E. N. Economou, *Phys. Rev.* **182**, 539 (1969).
- [59] R. B. Pettit, J. Silcox, and R. Vincent, *Phys. Rev. B* **11**, 3116 (1975).
- [60] R. Matz and H. Lüth, *Phys. Rev. Lett.* **46**, 500 (1981).
- [61] Y. Chen, S. Nannarone, J. Schaefer, J. C. Hermanson, and G. J. Lapeyre, *Phys. Rev. B* **39**, 7653 (1989).
- [62] G. Bell, T. Jones, and C. McConville, *Surf. Sci.* **405**, 280 (1998).
- [63] S. R. Streight and D. L. Mills, *Phys. Rev. B* **40**, 10488 (1989).
- [64] S. Fardad, E. Alexander Ramos, and A. Salandrino, *Opt. Lett.* **42**, 2038 (2017).
- [65] H. Morikawa and M. Fujita, *Thin Solid Films* **339**, 309 (1999).
- [66] A. Rogozin, N. Shevchenko, M. Vinnichenko, F. Prokert, V. Cantelli, A. Kolitsch, and W. Möller, *Appl. Phys. Lett.* **85**, 212 (2004).
- [67] J. H. Mooij, *Phys. Status Solidi A* **17**, 521 (1973).
- [68] J. R. Bellingham, W. A. Phillips, and C. J. Adkins, *J. Phys.: Condens. Matter* **2**, 6207 (1990).